Ion and electron beam assisted growth of nanometric Si_mO_n structures for near-field microscopy

E. J. Sánchez, J. T. Krug II, and X. S. Xie[a)]
Department of Chemistry and Chemical Biology, Harvard University, Cambridge, Massachusetts 02138

(Received 22 May 2002; accepted 13 August 2002)

We report the fabrication of nanometric, conformal, smooth dielectric coatings on the ends of apertureless near-field optical probes by both ion beam and electron beam assisted deposition techniques (IBAD and EBAD). The ion beam provides a higher Si_mO_n growth rate than the electron beam, though the undesirable implantation of Ga ions may outweigh the benefits of rapid growth. Wavelength dispersive x-ray spectroscopy reveals that the electron beam deposited dielectric has a stoichiometry of Si_nO_{2n}. We present two near-field optics applications of EBAD and IBAD grown dielectric layers. EBAD deposited coatings can be used to reduce fluorescence quenching in apertureless near-field scanning optical microscopy, while IBAD fabricated structures are suited for micro/nano-optics. © *2002 American Institute of Physics.* [DOI: 10.1063/1.1511801]

I. INTRODUCTION

Near field scanning optical microscopy (NSOM) extends optical measurements beyond the diffraction limit.[1–4] Typically, NSOM measurements are made with Al coated, tapered optical fibers, and yield resolutions on the order of ~50–100 nm.[4] Recent research in NSOM has demonstrated that apertureless probes can further improve spatial resolution to the sub-20 nm regime.[5–11] The apertureless technique involves the use of a metal tip of specific geometry in the presence of an electromagnetic field with proper excitation polarization. Strong evanescent fields are generated at the tip apex. These strong fields are used as a highly localized excitation source for a spectroscopic transition of interest.[9,10] The resolution limits attainable with this technique, ranging from ~10 to 20 nm, makes possible the study of closely packed chromophoric membrane proteins. In practice, the sample is scanned with respect to the probe, and the fluorescence is collected through the exciting objective. Unfortunately, the presence of the metal tip near the fluorophore leads to fluorescence quenching.[12] This results in a negative fluorescence image, essentially a dark spot at the chromophore position surrounded by a sharp halo of emission. Fluorescence quenching has limited apertureless NSOM fluorescence experiments to systems in which fast Förster energy transfer along molecular aggregates such as photosynthetic membranes competes with the fluorescence quenching.[10] Both the field enhancement and the fluorescence quantum yield change rapidly as a function of distance from the probe. There exists an optimal probe–fluorophore distance at which the excitation field enhancement is still high while quenching is reduced.[12,13] When probe–fluorophore distances are increased beyond this optimal distance, the rapidly declining excitation field generates little fluorescence signal. When the fluorophore is closer to the probe than the optimal distance, highly efficient quenching eliminates any fluorescence signal.

We modify apertureless NSOM probes with a combined focused ion beam (FIB) and scanning electron microscope (SEM) (DB235 DualBeam FIB/SEM manufactured by FEI) to circumvent the quenching problem. The FIB is capable of nanometer scale milling of complex geometries.[14] It has been a useful tool in the semiconductor industry,[15] for transmission electron microscope (TEM) sample cross-section thinning,[16] in biology,[16,17] and for scanning probe microscopy.[10,18] In addition to removing material, the system can also deposit metals and dielectrics while simultaneously imaging the sample. Although primarily used for prototype circuit repair, ion beam assisted deposition (IBAD) has been applied to the creation of a microcylindrical lens.[19] IBAD represents a better alternative to electron beam and optical lithographic techniques for the creation of micro-optics on complex three-dimensional (3D) geometries. Potential applications of this technique include the creation of waveguide structures fabricated directly on fibers, micro-optics for quantum computing, and micro-optical chemical sensors. Electron beam assisted deposition (EBAD) is analogous to IBAD, though the ion beam is supplanted by an electron beam to catalyze the deposition process. This switch to electron beam assisted deposition is important on several fronts which will be discussed below. Our interest is the creation of near-field optical probes capable of achieving sub-10 nm resolution in order to study closely packed proteins in photosynthetic membranes.[10,20] We present a technique to create homogeneous, nanometer scale silicon oxide coatings on near-field probes in order to minimize quenching.

We demonstrate the ability to grow a dielectric material on complex three-dimensional substrates using ion and electron beams. These techniques will be useful in fast prototyping of different optical probes on the nanometric scale. The benefits and drawbacks of using ion and electron beams will be presented.

[a)]Author to whom correspondence should be addressed; electronic mail: xie@chemistry.harvard.edu

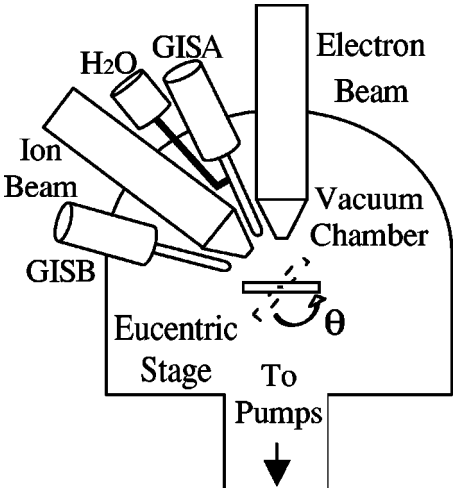

FIG. 1. Dual beam FIB/SEM chamber indicating the placement of ion and electron beams and gas injection systems. The GIS are used for IBAD and EBAD. GIS A contains TEOS and GIS B a Pt–organometallic precursor.

II. EXPERIMENTAL SETUP

The FIB system (FEI Strata DB-235) utilizes a liquid metal (Ga^+) ion gun source, accelerated to 30 kV and with specimen currents ranging from 1 pA to 20 nA. Although the field emitting tip is tungsten, it can be coated with a variety of elements (In, Au, etc.); Ga is the preferred material because of its high mass, stability, and low melting temperature (29 °C). Tip emission currents are systematically adjusted to a constant 2.2 μA to maintain the stability of the emitter[21] as well as extend the lifetime of the Ga reservoir and maintain a low energy spread. The system utilizes a two-lens, "stacked" electrostatic focusing column, and the minimum focused ion beam widths are determined by the current. One generally assumes a Gaussian beam profile although the profile at the focus is quite complex.[22] The secondary electrons liberated from the surface by the ions are collected for imaging. Beam currents are reduced to 1–30 pA for imaging in order to minimize damage by the ion beam, with spot sizes of ~3–25 nm. The field emission SEM allows for nondestructive, high resolution sample imaging during ion beam milling. Figure 1 shows the placement of the ion gun, electron gun, and gas injection systems (GIS) in the vacuum chamber. The ion gun, electron gun, and the gas injectors point to the eucentric point within the chamber for repeatable and fast changeover between imaging, milling, and deposition modes. The sample stage tilt range is $\Theta = -10°$ to $+60°$ (see Fig. 1), and the system requires no special sample preparation.

III. DEPOSITION SCHEMES

FIB systems have been available for over a decade for the purpose of semiconductor chip inspection. Recent technological improvements have allowed these units to perform repair functions; i.e., removing material to reach a defect region within a failed chip, rebuilding a specific conductive track(s), and depositing an insulating layer to isolate the conductive tracks. The rebuilding of an electrical track involves the deposition of a conductive material via injection of an organometallic precursor gas while scanning a given region with the ion beam. Metals that can be deposited in this fashion include Pt,[23,24] W,[24–26] Cu,[27] and Au.[28,29] Insulating layers of silicon oxides can also be deposited in a similar process, albeit with different precursors. The ideal insulator deposition process would yield pure SiO_2 in order to achieve very low conductivity. Different materials such as tetraethylorthosilicate (TEOS) ($Si(C_2H_50)_4$),[30,31] tetramethoxysilane,[32] and 1,3,5,7 tetramethylcyclotetrasiloxane[33,34] have been used as precursors. TEOS is easily decomposed in the presence of water, producing a hydrolyzed form of silicon compound and ethanol. In the Strata DB-235, the TEOS is heated to 28 °C to create the necessary vapor pressure for deposition (vapor pressure at 20 °C is 1.73×10^{-3} mbar). In TEOS, the silicon atom is preoxidized, therefore deposition does not require an oxidation reaction. One can use the Ga^+ beam to catalyze insulator deposition, but the ions are implanted into the insulator, leading to a slight increase in conductivity.[35,36] This ion implantation also results in a slight, but visible, gold coloration in the deposited material.

Although deposition is a complex process, some progress has been made toward the quantitative understanding of its characteristics. A model for ion assisted deposition was introduced by Petzold and Heard.[37] Although the model assumed deposition of an organometallic molecule onto a substrate, it can be extended to the growth of dielectric material, as the model is independent of the details of the chemical reaction. The following equation describes the deposition rate:

$$\frac{dn(t)}{dt} = g\Phi\left[1 - \frac{n(t)}{n_0}\right] - \frac{n(t)}{\tau_d} - \sigma n(t) i, \tag{1}$$

where n is the number of adsorbed molecules, n_0 the maximum number of adsorption sites available per monolayer (molecules/cm^2), Φ the gas flux to the substrate (molecules/cm^2), g the sticking coefficient of the molecules, τ_D the resident time of the precursor molecule at the surface, σ the ion collision cross section of the molecule, and i the ion flux rate of the exposed beam area (ions/cm^2 s). The first term in Eq. (1) is the adsorption rate of deposited molecules on the substrate. The second term represents the spontaneous desorption of molecules from the monolayer, with τ_m the mean lifetime of an adsorbed molecule. The third term is the rate of ion induced dissociation of the adsorbed molecules, where secondary electrons released from the surface by the ion beam interact with the absorbed molecules.[38] This rate equation, which assumes no surface diffusion, allows the determination of deposition rates (nm/s) for IBAD using experimental values.[37] For this work we did all deposition runs in one session on the system in order to have consistent growth rate data. The placement of structures with respect to one another was carefully chosen to minimize geometrical deposition interference.

IV. ION BEAM ASSISTED DEPOSITION (IBAD)

When depositing materials through IBAD, one must balance a variety of factors. Lower ion beam currents yield lower growth rates in general. Easily damaged surfaces often

necessitate the sacrifice of rapid deposition for the benefits of sample integrity. The IBAD growth rates are optimized with beam currents of 100–300 pA (spot sizes of roughly 30–50 nm, respectively) for delicate samples. Growth rates for beam currents less than 10 pA are extremely low. Growth rates at currents above 500 pA are also difficult to determine due to deep milling into the substrate. Deposition and imaging at these higher currents is not optimal, as the spot size can be over 500 nm wide. The base pressure of the chamber before deposition is $\sim 7.5\times 10^{-7}$ mbar. The injection of a gas for the deposition process causes an increase in chamber pressure. The TEOS causes an increase to 9×10^{-6} mbar and the co-injection of H_2O contributes an increase to the final pressure of 2×10^{-5} mbar at steady state. The gas flow is aimed directly at the point of growth from a vertical distance of ~ 140 μm, a horizontal offset distance of ~ 75 μm, and an angle of approximately 45° to the sample surface.

The beam overlap and dwell times are user inputs that strongly affect deposition rate. These digital parameters are applied to the point maps of user-defined patterns (squares, circles, quadrilaterals, etc.). The separation s between adjacent ion beam positions at a given beam overlap o for a beam full width at half maximum f is given by

$$S=f(1-o). \tag{2}$$

For example, for a beam current of 15 pA ($f\sim 20$ nm) and a beam overlap of 50% ($o=0.5$), the beam separation would be 10 nm. A beam overlap of 0% corresponds to a separation of 20 nm and −200% a separation of 60 nm. In our work we vary the beam overlap between 0% and −400%. The FIB computer calculates the expected beam width at the focus based on the beam current aperture chosen and determines the spatial beam separation for the object to be milled or deposited. The dwell time is defined as the time the beam remains on each fixed position in the pattern per pass.

For fixed gas flow, deposition is optimized by three deposition parameters: beam current, beam overlap, and dwell time. The first parameter, beam current, is directly related to beam focal width. A higher beam current results in a larger beam waist at the focus. Figure 2 shows the results of growth rate for two different overlaps (−200% and −300%). In both cases the deposition rate reaches saturation at roughly 300 pA at 0.1 μs dwell time. At higher currents, sample sputtering outpaces deposition. Therefore, we have fixed the beam current at 300 pA for the optimization of beam overlap and dwell time.

At this current, a series of glass pads were grown with different beam overlaps and dwell times. Figure 3 shows the volumetric growth rate (μm^3/min) as a function of beam overlap and dwell time, as needed for the optimization of IBAD growth using a 30 kV gallium beam. Shorter dwell times and greater beam spacing from point to point increase growth rate. If the dwell time is too long and beam overlap is high, substrate milling becomes dominant as seen in Fig. 3. The software of the Strata DB-235 precludes dwell times less than 100 ns. Increasing the beam overlap beyond −400% causes the growth to have voids and be less homogeneous. The graph of Fig. 3(a) indicates the maximum growth rate of 4.81 μm^3 at a −400% beam overlap with a fast dwell time of

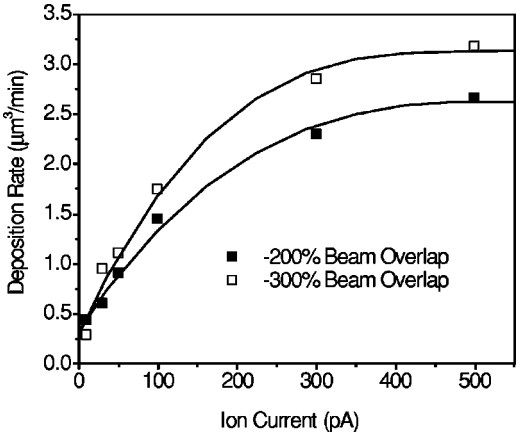

FIG. 2. IBAD growth rate as a function of milling current and beam overlap. The lines are curve fits for two different overlaps; −200% beam overlap (■), and for −300% (□) line. The pixel dwell time for these growths is 0.1 μs.

0.1 μs. Figure 3(b) is a composition of different growth runs to pictorally demonstrate the rate of growth. At lower beam overlaps the silicon substrate was sputtered badly during deposition, which can be seen in the lower part of Fig. 3(b). The break even point to get more deposition than etching of Si is approximately 0.6 μs pixel dwell time with a beam overlap of −100%. From the graph, one can determine the best ion beam overlap for maximum growth rate is approximately −400% with a beam dwell time per pixel of 0.1 μs.

Even modestly long beam dwell times can lead to significant milling and growth into a substrate. Initially the surface is milled; then deposition follows, leading to a volume under the deposited glass that contains a mixture of substrate, glass, and Ga. Figure 4(a) shows examples of good deposition using IBAD on a smooth substrate of Si at three different currents: (1) 300 pA, (2) 200 pA, and (3) 100 pA. Figure 4(b) shows the implantation of Ga ions into the surface of silicon. Area 1 of Fig. 4(b) is a mixture of Ga, Si, and TEOS decomposition product, yielding slightly different contrast on the secondary electron image. Once growth has been initiated, the subsequent glass grows with only Ga implantation.

Although relative growth rates for IBAD and EBAD parameters are fairly reproducible, the absolute growth rate is very sensitive to precursor flow. If some small structure or depression obstructs gas flow across the substrate, the growth rate can be significantly altered. In our experiments deposition was performed on clean, flat Si surfaces at least 5 μm from the closest structure, unless otherwise stated. Another important aspect to growing microstructures on rough surfaces is that growing at grazing incident angles can cause mushroom-like growth. Figure 5(a) shows the attempts at IBAD growth with different currents on a rough Al surface at 30° sample tilt. Figure 5(b) shows IBAD growth on an Al substrate at normal incidence. The smoothness of the normal incidence deposition can be easily seen, even on the rough surface. To avoid rough coatings on complex objects, care must taken to make a surface perpendicular to the beam. The rough coating is possibly due to uneven flow of the gas causing vortices or reduced precursor coverage in some areas.

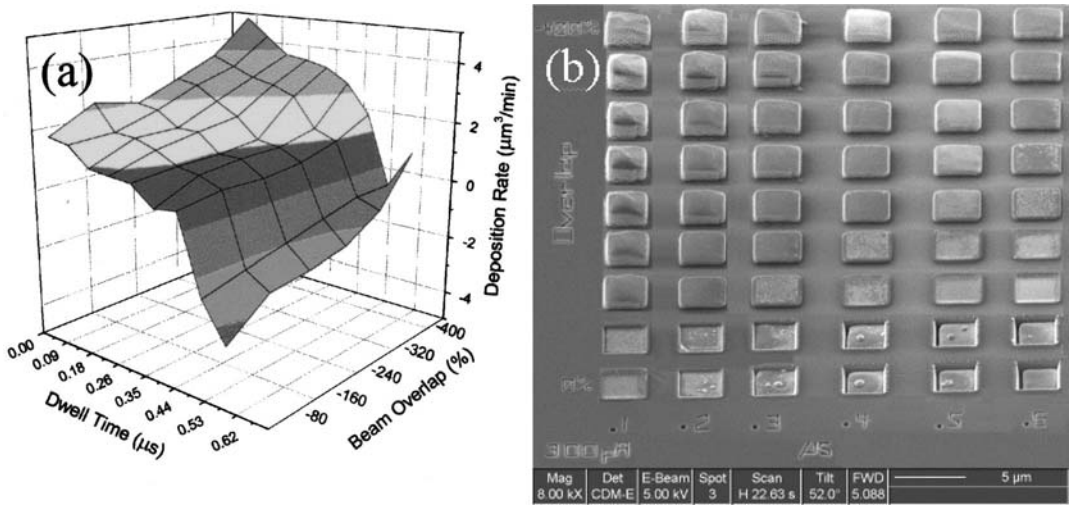

FIG. 3. (a) Growth rate of IBAD as a function of dwell time and beam overlap (in μm^3/min). (b) SEM micrograph of IBAD growth of Si_mO_n on a Si substrate as a function of overlap (vertical, overlap increases from top to bottom) and dwell time (horizontal, increasing dwell time from left to right).

Growing with the beam on a smooth surface or with the beam perpendicular to the surface generates a much smoother coating. This is important when attempting to make dielectric objects with no voids. Sample position drift can be another cause of uneven insulator deposition. In our system, lateral position drift can be as low as 6.5 nm/min (determined on a Si substrate at 15 kV, 30 pA). When building insulating dielectrics, the drift can be greater as a result of charging of the deposited material. Less drift occurs with IBAD than with EBAD because Ga^+ ion implantation creates potential electron leak pathways.

V. ELECTRON BEAM ASSISTED DEPOSITION (EBAD)

The field emission electron column (based on a Philips XL-40 electron column) has an imaging resolution better than 2 nm. The electron beam utilizes beam currents of 5 pA–2 nA. EBAD represents an application of the general techniques of IBAD to the deposition of materials with the electron beam. The same precursor materials (TEOS, water vapor) are introduced via a gas injection system near the sample surface, and the electron beam is scanned over the area to be coated with the dielectric. As with IBAD deposition, the most important parameters for growth rate determination are beam current, beam overlap, and dwell time. In addition, the electron beam accelerating voltage plays a critical role. Since growth primarily occurs through secondary electron interaction with the precursor gas,[32] lower beam voltages, which have an interaction volume close to the surface, are more desirable. Unfortunately, lower voltages lead to worse spatial resolution and susceptibility to stray fields and charging. A voltage of 2 kV was chosen to be the compromise voltage. A method of growth rate optimization similar to that used with IBAD was used for the EBAD technique. Glass pads were grown using EBAD for 10 min at a base pressure similar to that of IBAD. Due to slight charging-induced sample drift over a 10 min period, the area of illumination is rechecked and repositioned during growth to maintain constant position. Figures 6(a) and 6(b) show graphs of volumetric growth rate as a function of beam overlap and dwell time taken at two different currents (245 pA and 2 nA). Similar to IBAD, the beam current is selected by beam aperture size. Figure 6(b) shows that a growth rate maximum of 2.1 μm^3/min (at a 2 nA beam current) is obtained for a short dwell time (0.2 μs) and large overlap (-200%). Similar to the ion beam, the highest growth rates occur when the dwell time is short and the overlap is optimized for specific beam coverage. Another group using TEOS and an electron beam for dielectric deposition had growth rates slightly lower than ours.[31] They had maximum growth rates around ~ 0.5 μm^3/min for a beam voltage of 3

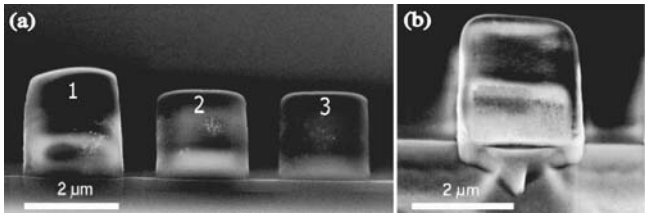

FIG. 4. (a) SEM side cross sections of SiO_2 IBAD grown pads on Si substrate at: (1) 300 pA, (2) 200 pA, and (3) 100 pA for 5 min. (b) SEM side cross section of an IBAD grown SiO_2 pad at 300 pA and long dwell time of 5 μs, showing the back etching and implantation (region 1) into the substrate until growth of dielectric occurs (region 2).

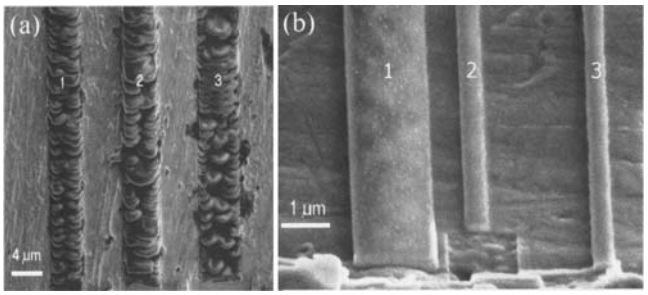

FIG. 5. (a) IBAD growth of SiO_2 on a rough Al substrate at three different currents: (1) 100 pA, (2) 200 pA, and (3) 300 pA. The incident deposition angle was 30° to the surface. (b) Glass growth of three lines at a near normal incidence deposition angle on a similar substrate at a current of 300 pA.

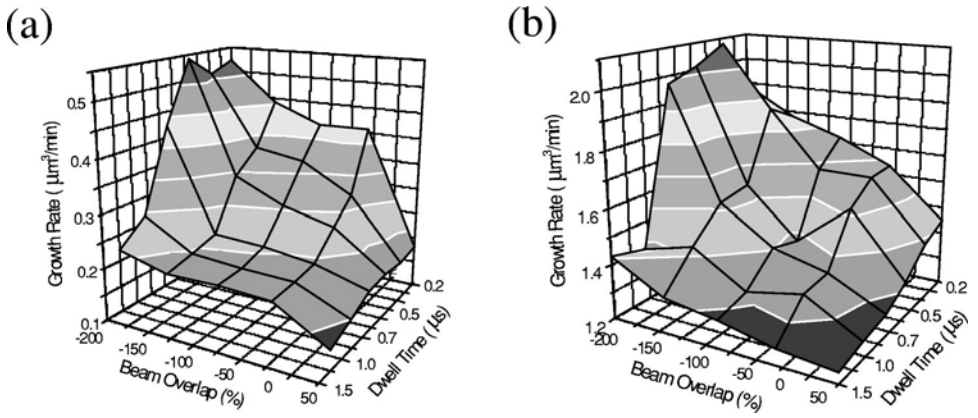

FIG. 6. EBAD growth of SiO_2 on Si substrate at different beam overlaps and dwell times at: (a) 245 pA and (b) 2 nA electron currents.

kV and a beam current of 8–15 nA (XL-830 Dual-beam). We achieve slightly higher rates at lower voltages and lower currents, but also possibly different gas flux.

While IBAD generally yields higher deposition rates than does EBAD, a variety of factors may make EBAD preferable in some circumstances. First, the use of the electron beam as opposed to the ion beam precludes significant sample damage for all but the most delicate surfaces. Second, EBAD could be applied by any SEM with the simple addition of a gas injection system. Finally, the use of the electron beam should avoid any contamination of the deposited material with undesirable ions. This compositional advantage of EBAD is examined in Sec. VI.

VI. GROWTH COMPOSITION ANALYSES

We used energy dispersive spectroscopy (EDX) (Noran-Advantage EDX with a diamond window on a Leo-982 FESEM) to analyze the magnitude of ion implantation. This EDX analysis was performed without standards and was considered to be only qualitative. We were able to determine the elemental percentage as Ga: Si: O (20:20:60) at multiple beam currents ranging from 100 to 500 pA. Within this range of beam currents there was no significant difference in composition. Previous work by Young and Puretz[30] showed the EDX-determined elemental composition as (Ga: Si: O: C of 13: 11: 64: 11 at. %), which agrees with our EDX analysis. The presence of carbon was expected, as hydrocarbon growth can occur as a result of normal beam exposure to residual pump oil, etc. in the chamber. Our sample was annealed in a furnace in the presence of argon at 600 °C for 30 min, which seems to have eliminated our carbon signal. Our data indicate much higher gallium implantation. However, Young's analysis did not specify growth parameters and did not use water to further decompose TEOS. The reasons for the higher oxygen reading than our wavelength dispersive spectroscopy (WDX) values may be due to the lack of calibration standards used in the analysis.

Using a scanning Auger system, Lipp *et al.*[32] determined a composition of equal percentage for both Si (42%) and O (40%) but also saw a large C (18%) content. Their precursor was tetramethoxysilane–$C_4H_{12}O_4Si$. It is possible that due to the use of the different precursor, there is a higher percentage of hydrocarbons in the deposition. Another reason for the high carbon content could be that the interaction volume for Auger is much closer to the surface, where more hydrocarbon contaminants might be located. This shallow interaction volume may mask bulk composition.

We utilized WDX (Cameca MBX with a Noran TN-1310 WDS) in order to quantitatively determine the stoichiometry of the deposited materials. With this method we determined that the IBAD deposited growth is high in Ga.[39] WDX indicated a normalized atom percent of Ga:Si:O of 33:16:51. Our data were obtained on a nickel substrate to ease separation of adjacent spectral peaks. Standards were used for calibration of the detected signals, leading to a much more accurate analysis than EDX. The IBAD growth conditions were optimized for maximum growth rate, with an ion beam current of 300 pA. The EBAD composition data were taken on a 5 μm$\times$5 μm electron exposed area. The composition of the insulator using EBAD was only determined by WDX. The deposition conditions were an electron beam current of 2 nA, 2 kV beam voltage, beam overlap of -50%, and a pixel dwell time of 0.7 μs. After analysis of several EBAD grown glass pads, the stoichiometry was consistently determined to be Si_nO_{2n}. Based on the composition we make the assumption in the design of the near-field probes that the material has dielectric constants similar to that of fused silica.

VII. APPLICATION TO NEAR-FIELD OPTICS

Once the optimal growth parameters were determined, we set forth to create nano-optics. Rapid prototyping can be achieved with EBAD and IBAD without special preparation, as required with electron beam lithography. This deposition

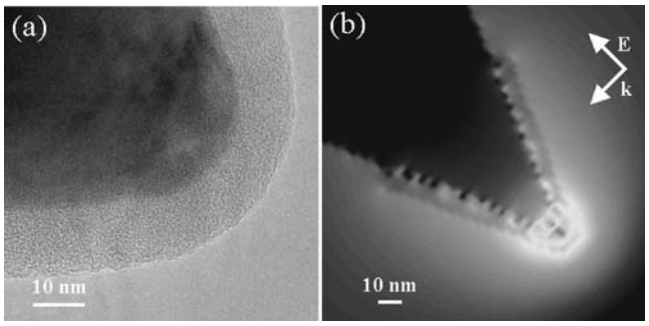

FIG. 7. (a) TEM micrograph of metal tip with an EBAD grown SiO_2 overlayer (taken with a JEOL model JEM-2010F), (b) 3D FDTD modeling of the total electric field of a Au tip with a 9 nm thick glass coating. The finite cell size (3 nm) causes the apparent field modulation.

can also be quickly performed on complex 3D objects. Others have successfully ion milled diffraction optical elements into glass substrates and created microcylindrical optical elements.[19] When creating complex structures on small objects such as scanning probe tips, it is important not to grow at large currents. Otherwise the initial beam passes will sputter through the thin sections of the substrate and improper growth of the dielectric will occur.

Using EBAD, we were able to create a dielectric film with nanometer conformity over a complex geometry. Figure 7(a) shows an electron micrograph of the SiO_2 overlayer on a metal tip. In detecting the fluorescence signal from a molecule the optimum distance from the chromophore to the metal surface would be approximately 22 nm (for a parallel emitting dipole) or 24 nm (for a perpendicular emitting dipole) with a minimum distance of 3 or 5 nm, respectively. If the metal tip is closer than the 3–5 nm distances, then the fluorescence in dramatically quenched, leading to no detected signal.[13]

We use electromagnetic modeling to optimize near-field tip design using the finite difference time domain (FDTD) technique,[40] which has proven to be very useful for NSOM optics.[41,42] In order to model any arbitrary geometry, the object is divided into cubic cells[43] with the appropriate frequency dependent susceptibility. The electric field in each cell is under plane wave illumination through time domain integration of Maxwell's equations.[44] An absorbing boundary condition is used.[45] Figure 7(b) shows the FDTD modeling of the metal tip with a 9 nm glass layer. The incident excitation field in Fig. 7(b) was set to field strength of 1 V/m at 800 nm wavelength, and the space is discretized with 3 nm cubes. The material of the tip is Au, and the spacer is SiO_2. The intensity enhancement at the end of the tip is 100 without the spacer, approximately 5 nm in front of the tip. When the SiO_2 spacer of 9 nm is present, the enhancement is reduced to 50; this is still high enough for near-field imaging at 5 nm in front of the tip.

Normally, apertureless near-field optical probes require direct illumination of the tip apex in order to generate a subdiffraction limited light spot. A large background signal originates from the emission of many chromophores in the illuminated volume. Typically, one uses a tip with a high field enhancement in order to overcome the background contribution. Another way to overcome this problem would be to nonradiatively propagate a field to the end of the tip where the energy of the field could emit radiatively, thereby eliminating the background contribution. We designed a tip with the Otto geometry to generate resonant surface plasmons.[46] Figure 8(a) is the electron micrograph of this surface plasmon resonance (SPR) tip, built by the combination of milling and IBAD of TEOS. Figure 8(b) shows the electron micrograph of the tip after final milling. This tip generates plasmons microns away from the tip end and nonradiatively propagates the energy to the tip end. The angle of the prism, tip shaft length, and the gap between the prism and the metal has been carefully calculated using Fresnel equations for a three-layer system in order to achieve resonance, which can generate a very high field. When the plasmon reaches the tip end it generates a strong evanescent field within a region on the order of the tip end diameter. The advantage is the elimination of signal generated by far-field illumination, and subsequent increase in the signal to background ratio. In creating this tip, it was necessary to carefully plan each cut in 3D in order to minimize time of FIB milling and maximize the quality of the prism. The utility of such probes is currently under investigation.

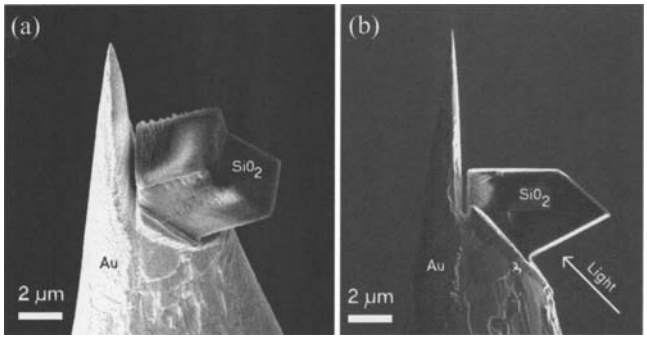

FIG. 8. SPR tip using the Otto attenuated total reflection technique: (a) SEM micrograph of an ion milled and IBAD grown glass prism on a Au etched tip and (b) side view after final cutting with the FIB. The field enhancement at the tip end is 50. The polarization and propagation direction of the incident field are shown.

VIII. DISCUSSION

We have determined the composition of glass grown with IBAD as Ga:Si:O–33:16:51 and EBAD as SiO_2. The composition is similar to literature values when measured with EDX qualitative analysis, but differs greatly in atom percent when the more accurate quantitative method (WDX) is used. We have optimized glass deposition based on electron beam parameters: voltage, current, beam overlap, and dwell time. We have shown that a nanometrically smooth dielectric material can easily be applied to an apertureless tip in order to achieve high spatial resolution fluorescence spectroscopy without significant quenching. The EBAD technique can be applied to any SEM with a spare chamber port for gas injection. The electron beam growth rate can be comparable to that of the ion beam and without Ga contamination. However, the IBAD may be desirable where a metal impurity is not so critical, and fast growth rates are desired. We have applied these growth techniques to different types of near-field probes in order to achieve subdiffraction imaging. The IBAD and EBAD techniques are well suited for a variety of nano-optics applications.

ACKNOWLEDGMENTS

The authors would like to thank the U.S. Department of Energy Basic Energy Science Division for funding this work, and National Science Foundation and the Center for Imaging and Mesoscale Structures (CIMS) at Harvard for funding of the FIB. They would also like to thank FEI for their excellent technical support, David Lang for WDX assistance, Yuan Lu, and Warren Moberly-Chan for help with TEM/EDX analysis.

[1] D. W. Pohl, W. Denk, and M. Lanz, Appl. Phys. Lett. **44**, 651 (1984).
[2] A. Lewis, M. Issacson, A. Harootunian, and A. Murray, Ultramicroscopy **13**, 227 (1984).

[3] A. Harootunian, E. Betzig, M. Iasscson, and A. Lewis, Appl. Phys. Lett. **49**, 674 (1986).
[4] E. Betzig, J. K. Trautman, T. D. Harris, J. S. Weiner, and R. L. Kostelak, Science **251**, 1468 (1991).
[5] S. Kawata and U. Inouye, Ultramicroscopy **57**, 313 (1995).
[6] W. Denk and D. W. Pohl, J. Vac. Sci. Technol. B **9**, 510 (1991).
[7] F. Zenhausern, M. P. O'Boyle, and H. K. Wickramasinghe, Appl. Phys. Lett. **65**, 1623 (1994).
[8] J. Jersch and K. Dickmann, Appl. Phys. Lett. **68**, 868 (1996).
[9] L. Novotny, E. J. Sanchez, and X. S. Xie, Ultramicroscopy **71**, 21 (1998).
[10] E. J. Sanchez, L. Novotny, and X. S. Xie, Phys. Rev. Lett. **82**, 4014 (1999).
[11] A. A. Gorbonuv and W. Pompe, Phys. Status Solidi A **145**, 333 (1994).
[12] R. R. Chance, A. Prock, and R. Silbey, J. Chem. Phys. **62**, 2245 (1975).
[13] P. T. Leung and T. F. George, J. Chem. Phys. **85**, 4729 (1986).
[14] R. L. Gerlach and M. Utlaut, Proc. SPIE **4510**, 96 (2001).
[15] R. J. Young, Microstruct. Sci. **25**, 491 (1998).
[16] L. A. Giannuzzi, J. L. Drown, S. R. Brown, R. B. Irwin, and F. A. Stevie, Microsc. Res. Tech. **41**, 285 (1998).
[17] R. J. Young, P. D. Carleson, X. Da, T. Hunt, and J. F. Walker, Proceedings of the International Symposium for Testing and Failure Analysis, Dallas, TX, November 15–19, 1998, pp. 329–336.
[18] J. E. Griffith, D. A. Grigg, M. J. Vasile, P. E. Russell, and E. A. Fitzgerald, J. Vac. Sci. Technol. A **10**, 674 (1992).
[19] F. Yongqi, N. K. A. Bryan, N. P. Hung, and O. N. Shing, Rev. Sci. Instrum. **71**, 1006 (2000).
[20] R. C. Dunn, G. R. Holtom, L. Mets, and X. S. Xie, J. Phys. Chem. **98**, 3094 (1994).
[21] L. W. Swanson, Appl. Surf. Sci. **76**, 80 (1994).
[22] J. Orloff, J. Z. Li, and M. Sato, J. Vac. Sci. Technol. B **9**, 2609 (1991).
[23] T. Tao, W. Wilkinson, and J. Melngailis, J. Vac. Sci. Technol. B **9**, 162 (1991).
[24] A. J. DeMarco and J. Melngailis, J. Vac. Sci. Technol. B **19**, 2543 (2001).
[25] Y. Madokoro, T. Ohnishi, and T. Ishitani, Proc. SPIE **1263**, 62 (1990).
[26] M. H. F. Overwijk and F. C. van den Heuvel, Nucl. Instrum. Methods Phys. Res. B **80–81**, 1324 (1993).
[27] A. D. della Ratta, J. Melngailis, and C. V. Thompson, J. Vac. Sci. Technol. B **11**, 2195 (1993).
[28] G. M. Shedd, H. Lezec, A. D. Dubner, and J. Melngailis, Appl. Phys. Lett. **49**, 1584 (1986).
[29] P. G. Blauner, A. D. Dubner, and A. Wagner, Proc. SPIE **1924**, 89 (1993).
[30] R. J. Young and J. Puretz, J. Vac. Sci. Technol. B **13**, 2576 (1995).
[31] G. Zimmermann and R. Chapman, Proceedings of the International Symposium for Testing and Failure Analysis, Santa Clara, CA, November 14–18, 1999, pp. 311-316.
[32] S. Lipp, L. Frey, C. Lehrer, B. Frank, E. Demm, S. Pauthner, and H. Ryssel, J. Vac. Sci. Technol. B **14**, 3920 (1996).
[33] H. Komano, H. Nakamura, M. Kariya, and M. Ogasawara, Proc. SPIE **2723**, 46 (1996).
[34] K. Edinger, J. Melngailis, and J. Orloff, J. Vac. Sci. Technol. B **16**, 3311 (1998).
[35] A. J. Steckl, H. C. Mogul, and S. M. Mogren, J. Vac. Sci. Technol. B **8**, 1937 (1990).
[36] J. Melngailis, *Research Laboratory Electronics* (Massachusetts Institute of Technology, Cambridge, MA, 1992), p. 27.
[37] H. C. Petzold and P. J. Heard, J. Vac. Sci. Technol. B **9**, 2664 (1991).
[38] S. Lipp, L. Frey, C. Lehrer, E. Demm, S. Pauthner, and H. Ryssel, Reliability Electron Devices, Failure Physics Analysis, Proceedings of the European Symposium, 1996, pp. 1779–1782.
[39] J. Goldstein, D. Newbury, and P. Echlin, Scanning Electron Microscopy and X-Ray Microanalysis, Book 1 (1984).
[40] A. Taflove and M. E. Brodwin, IEEE Trans. Microwave Theory Tech. **23**, 623 (1975).
[41] R. X. Bian, R. C. Dunn, X. S. Xie, and P. T. Leung, Phys. Rev. Lett. **75**, 4772 (1995).
[42] H. Nakamura, T. Sato, H. Kambe, K. Sawada, and T. Saiki, J. Microsc. **202**, 50 (2001).
[43] K. S. Yee, IEEE Trans. Antennas Propag. **14**, 302 (1966).
[44] J. T. Krug II, E. J. Sanchez, and X. S. Xie, J. Chem. Phys. **116**, 10895 (2002).
[45] R. J. Luebbers, F. Hunsberger, and K. S. Kunz, IEEE Trans. Antennas Propag. **39**, 39 (1991).
[46] A. Otto, Z. Phys. **216**, 398 (1968).